Solar Physics (2006) 235: 75–86
DOI: 10.1007/s11207-006-0049-x

SPECTRO-POLARIMETRIC OBSERVATIONS AND NON-LTE MODELING OF ELLERMAN BOMBS

HECTOR SOCAS-NAVARRO*
High Altitude Observatory, NCAR†, U.S.A.
(e-mail: navarro@ucar.edu)

VALENTÍN MARTÍNEZ PILLET
Instituto de Astrofísica de Canarias, La Laguna, Spain

and

DAVID ELMORE*, ANNA PIETARILA, BRUCE W. LITES,
and RAFAEL MANSO SAINZ
High Altitude Observatory, NCAR

(Received 16 August 2005; accepted 13 February 2006)

Abstract. Ellerman bombs are bright emission features observed in the wings of Hα, usually in the vicinity of magnetic concentrations. Here we show that they can also be detected in the Ca II infrared triplet lines, which are easier to interpret and therefore allow for more detailed diagnostics. We present full Stokes observations of the 849.8 and 854.2 nm lines acquired with the new spectro-polarimeter SPINOR. The data show no significant linear polarization at the level of 3×10^{-4}. The circular polarization profiles exhibit measureable signals with a very intricate pattern of peaks. A non-LTE analysis of the spectral profiles emerging from these features reveals the presence of strong downflows ($\sim$10 km s^{-1}) in a hot layer between the upper photosphere and the lower chromosphere.

1. Introduction

One of the most intriguing discoveries made in solar physics early in the last century was the phenomenon known as Ellerman bombs (EBs). The common use of the Hα line to monitor the Sun allowed the discovery of features with enhanced emission peaks in the wings of this line, not affecting the central absorption core (Ellerman, 1917). Off-band ($\sim$0.1 nm) Hα filtergrams showed these features to be spatially point-like structures with a size of $\sim 1''$, lasting for little more than 10 minutes (see Qiu *et al.*, 2000 and references therein). As they are virtually absent from line core filtergrams, they have always been associated with events taking place in the low chromosphere. This is also confirmed by their clear correlation with brightenings

*Visiting Astronomers, National Solar Observatory, operated by the Association of Universities for Research in Astronomy, Inc. (AURA), under cooperative agreement with the National Science Foundation.

†The National Center for Atmospheric Research (NCAR) is sponsored by the National Science Foundation, USA.

seen in the 160 nm continuum images from the TRACE satellite (Qiu *et al.*, 2000). Sometimes, an X-ray transient brightening can also be observed at the same location (Shimizu *et al.*, 2002). Recent reviews on EBs are given by Rust (2001) and in the introduction of Georgoulis *et al.* (2002).

The physical process behind EBs has remained elusive. The blue asymmetry observed by the Hα profiles (excess emission in the blue wing) has sometimes been associated with outward motions of solar material (Koval and Severny, 1970). But using two-component models separated along the line of sight, Dara *et al.* (1997) showed that the asymmetry could originate from either hot emitting material moving upwards or cold absorbing material falling from the top of the chromosphere. The relation to the magnetic field configuration has been controversial as well. EBs have been detected in two distinct solar magnetic scenarios, but always inside active regions. They occur in emerging regions between the opposite polarity footpoints and also surrounding isolated sunspots, beyond the penumbral boundary. For this later case, Nindos and Zirin (1998) have shown that they can be identified with the so-called Moving Magnetic Features (MMFs) that are seen in the moat region around sunspots (for a description of MMFs see Harvey and Harvey, 1973). Whereas this points towards a magnetic origin of EBs, a number of events observed by Nindos and Zirin (1998) (see also Dara *et al.*, 1997) were not clearly linked to magnetic structures. These authors point out that a number of cases showed a relationship with the boundaries of magnetic regions but others did not.

More recently the situation has been clarified by the analysis of the observations made by the Flare Genesis balloon experiment (Georgoulis *et al.*, 2002; Pariat *et al.*, 2004). Observing an emerging flux region, these authors describe dipolar features that appear in the middle of the region, where the flux emerges at the surface (below the so-called arch-filament system). With better sensitivity magnetograms than the previous work, Georgoulis *et al.* (2002) found that almost all EBs studied could be identified with the neutral line above dipolar features (or in neutral lines inside supergranular boundaries). Those cases not linked with the presence of neutral lines could be associated with interacting field lines above the photosphere, a result confirmed by the extrapolations made by Pariat *et al.* (2004). These authors proposed, then, as the most probably mechanism for the generation of EBs, some form of magnetic reconnection in the low chromosphere. That reconnection happens efficiently at these heights is supported by the fact that the temperature minimum is the region with the lowest electrical conductivity, and resistive processes occur there more easily than elsewhere (Litvinenko, 1999). While the Flare Genesis observations correspond to the central portion of an emerging active region, these conclusions offer an interesting parallelism with the EBs observed surrounding sunspots and associated to MMFs.

Pariat *et al.* (2004) pointed out that many of the bombs studied were located at the dipped portions of undulatory field lines in the flux emerging area. This undulatory or serpentine configuration is also used for the explanation of MMFs (as first proposed by Harvey and Harvey, 1973). In this way, a unifying scenario for

the generation of these point-like energy release processes could be constructed. But a study similar to that made by Pariat *et al.* (2004) for the moat of sunspots is still lacking. The comparison between the EBs seen in these two scenarios and the determination of their physical origin awaits more solid observational tools than Hα line profiles.

In particular, techniques providing information of the magnetic field at the chromospheric heights where the energy release takes place will be of great value. Hα linear polarization signals observed in EBs have been reported in the past (Rust and Keil, 1992), but their exact amount and origin remains controversial. In this paper, we propose the use of full Stokes spectropolarimetry in more reliable diagnostic lines such as the Ca II infrared triplet lines. The most important advantage these lines offer is the availability of powerful inversion techniques that can be used to cover almost the full chromospheric region. This paper presents a first characterization of the atmosphere of two regions close to a sunspot that display the properties ascribed to EBs.

2. Observations

The observations used in this work are first-light data from the new instrument Spectro-Polarimeter for INfrared and Optical Regions (SPINOR, see Socas-Navarro *et al.*, 2005), at the Dunn Solar Telescope (DST) located at the National Solar Observatory in Sunspot, NM. The dataset contains the two chromospheric Ca II lines at 849.8 and 854.2 nm and two photospheric Fe I lines at 849.7 and 853.8 nm. We observed active region NOAA 0634 on June 16 2004 at 15:16 UT, carrying out a 350-step scan with a spatial step of $0.22''$. By using the adaptive optics system of the DST (Ren *et al.*, 2003), we attained a spatial resolution as good as $0.6''$, although this figure varies slightly along the scanning direction (the horizontal direction in the figures) due to temporal variations of seeing.

In order to improve the signal-to-noise ratio in the Stokes profiles, we averaged the observations in 3×3 pixel ($0.66'' \times 1.2''$) boxes. The noise is thus reduced to $\sim 3 \times 10^{-4}$ times the continuum intensity. At this level there is barely any signal in Stokes Q and U, so we decided to leave them out of our analysis. The chromospheric Stokes V profiles, however, reveal fascinatingly complex shapes with multiple peaks, while the photospheric lines exhibit the usual antisymmetric profiles.

Figure 1 shows maps of the continuum intensity and a "magnetogram" taken in one of the photospheric lines. The magnetic configuration surrounding the sunspots appears very different on both sides of it. The western side exhibits a much more complex topology with an intricate pattern of plage fields extending from the sunspot boundary to the edge of the field of view. Hα images of the region (Figure 2) reveal considerable emission near the western penumbral boundary.

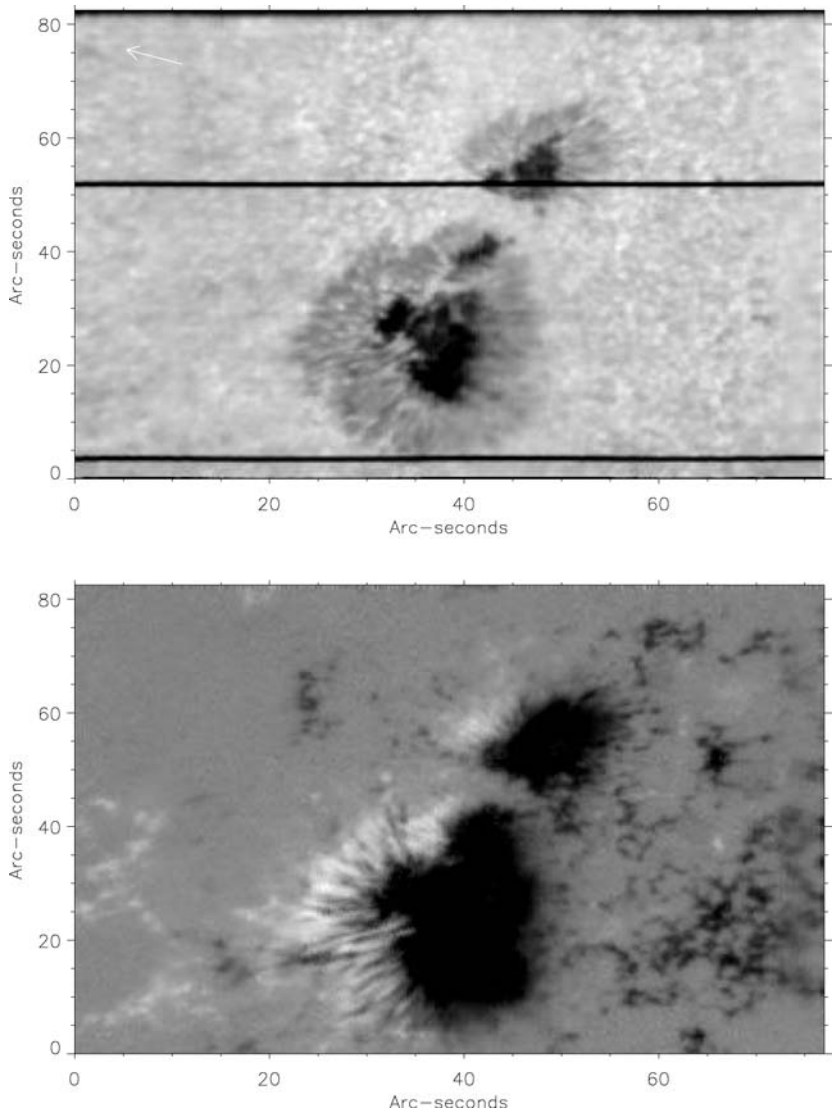

Figure 1. Top: Continuum map reconstructed from the spectro-polarimetric observations. North is up and West is to the right of the image. The arrow indicates the direction to the solar limb. *Bottom*: Circular polarization in the red lobe of the photospheric Fe I line at 849.7 nm. The horizontal dark stripes are hairlines inserted across the slit to serve as a reference for the calibration.

2.1. VELOCITIES

Photospheric velocity maps of NOAA 0634 were obtained by measuring the position of the minimum intensity of the Fe I line at 849.7 nm. A similar strategy is not viable for the Ca II lines, however, because of the complicated patterns of emission

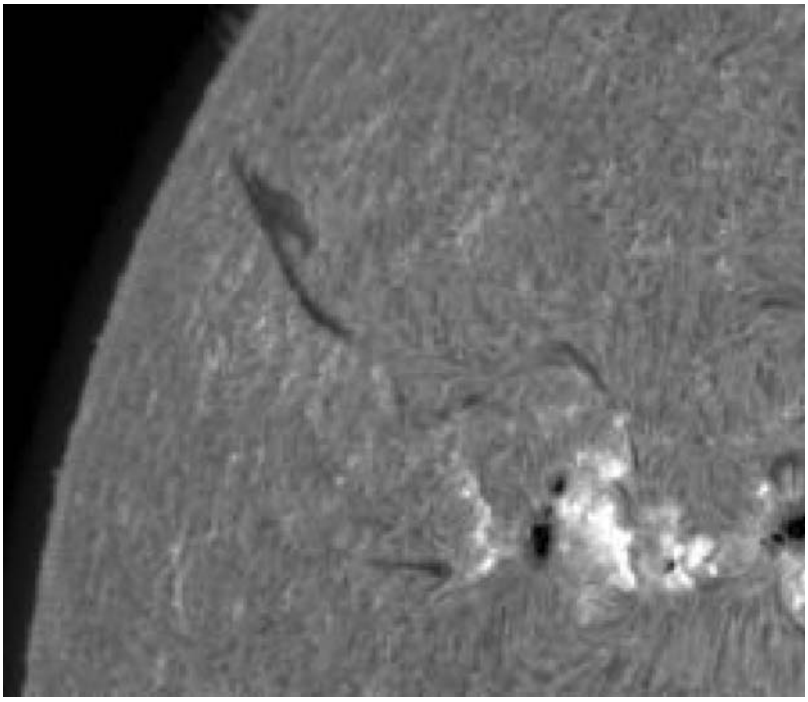

Figure 2. BBSO Hα image of NOAA 0634 taken on 16 June 2004 at 15:50 UT. Note the bright emission on the western side of the sunspot, near the penumbra.

reversals and self-absorptions found in the line cores. Instead, we measured the intensity difference between two points symmetrically located at various distances from the line core. This method is only an approximation but it works better than taking the minimum intensity position.

Figure 3 shows the velocity maps obtained at two heights, with the convention that positive velocities are away from the observer. The cosine of the heliocentric angle (μ) for this region is 0.71. Notice the two prominent bright features marked with arrows in the lower panel of the figure. These features are strong plasma flows directed away from the observer along the line of sight and located on the disk-center side of the sunspot (but outside the photospheric penumbral boundary). Detailed profiles of these features are shown in Figure 4.

Both features exhibit very strong redshifts, visible in Stokes I and V. Point A shows a very prominent redshift starting near 40 pm away from line center (corresponding roughly to the high photosphere or low chromosphere) all the way to the line core (middle chromosphere). This feature is well localized (see lower panel) and the Doppler shift is $\sim$14 km s^{-1}. Point B exhibits somewhat weaker flows ($\sim$10 km s^{-1}) which are more localized in height (upper photosphere/lower chromosphere), but has a more extended tail along the slit (see lower panel). Notice how both points A and B coincide with Hα emissions in Figure 2.

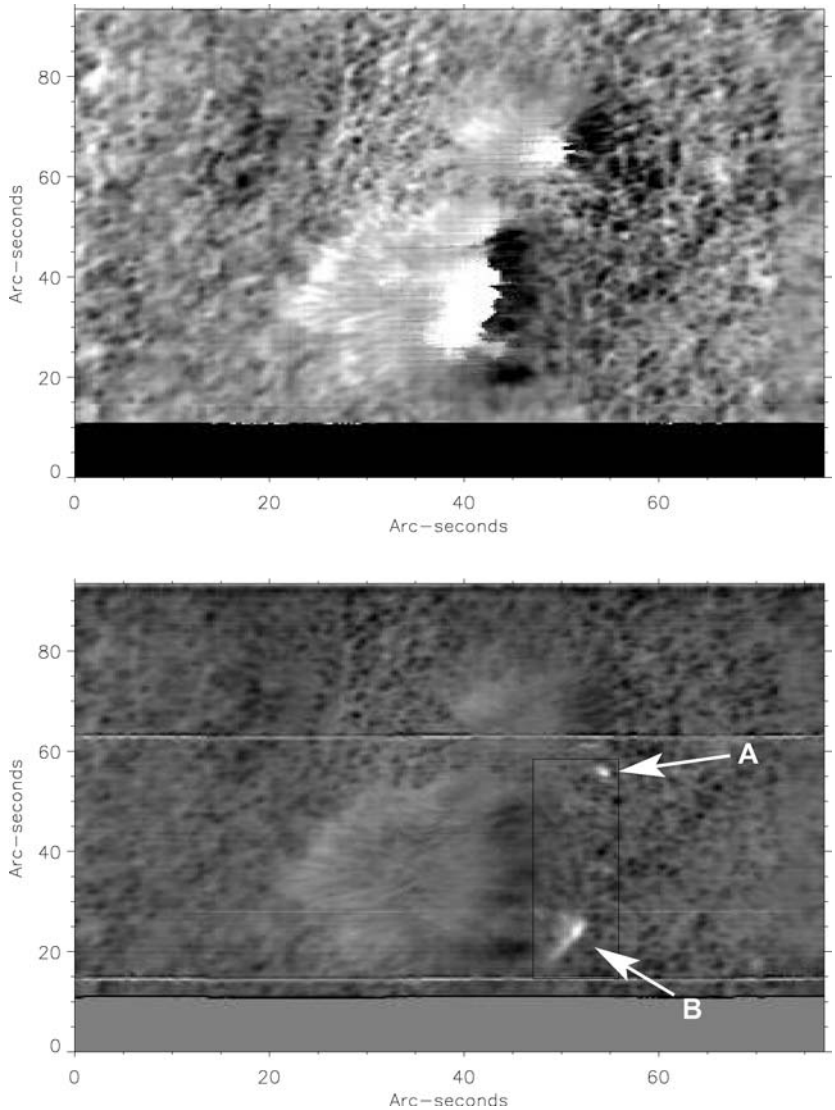

Figure 3. Top: Velocity map (arbitrary units) measured as the shift of Fe I 849.7 nm line core. In this paper we follow the astrophysical convention that positive values correspond to redshifts. *Bottom*: Dopplergram obtained by subtracting the intensity at two symmetric positions of the Ca II line at 849.8 nm. The positions measured are 0.135 nm apart, in the wings of the Ca II line. The photospheric character of both maps is evident from the granulation pattern. The areas marked by arrows and labeled *A* and *B* in the figure exhibit strong ($\sim$10 km s^{-1}) flows and have been subjected to detailed analysis in this work.

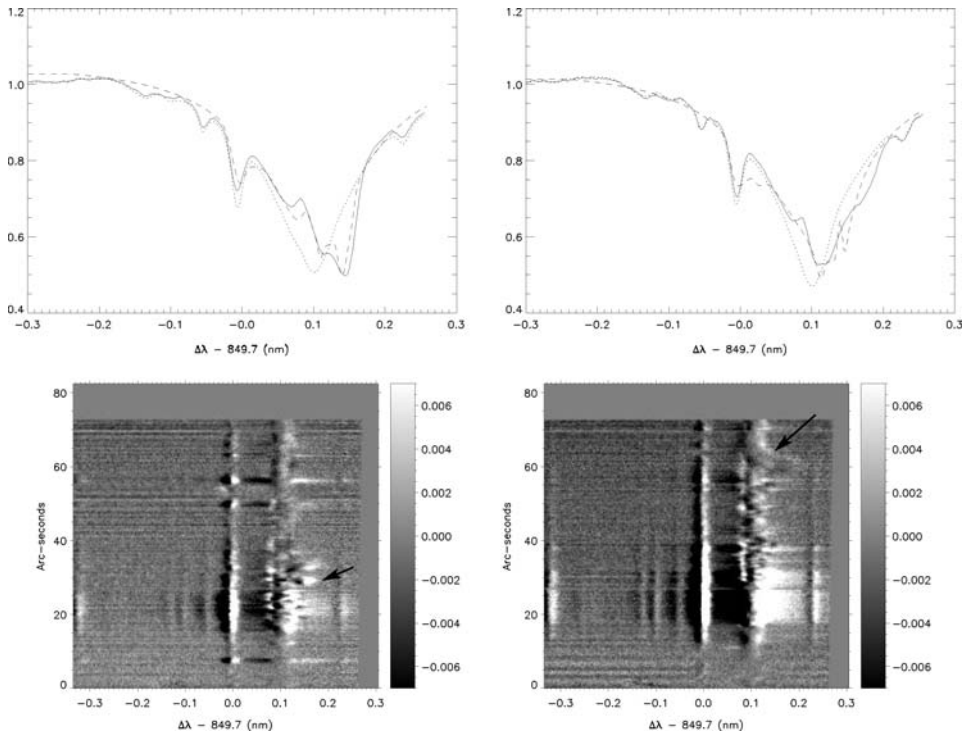

Figure 4. Top: Two sample profiles of the Ca II line at 849.8 nm observed in areas *A* (*left*) and *B* (*right*). These profiles exhibit particularly striking downflows. The *dashed line* shows the fit from the non-LTE inversion. Overplotted in *dotted line* for reference is the average profile along the slit direction. *Bottom*: Stokes *V* spectra along the slit. The *arrows* mark the position of the profiles shown in the upper panels.

3. Non-LTE Inversions

We performed detailed non-LTE inversions of the area surrounding points *A* and *B* in Figure 3. The inversions were carried out with the code of Socas-Navarro, Trujillo Bueno, and Ruiz Cobo (2000b) (see also Socas-Navarro, Ruiz Cobo, and Trujillo Bueno, 1998) by applying it systematically to each pixel independently. In order to minimize the risk of the algorithm settling on a secondary minimum, we repeated each inversion ten times with randomized initializations. The model atmosphere that yields the best fit to the observed Stokes profiles is taken as a good representation of the solar atmosphere under study.

The inversion code treats the Ca II lines in non-LTE and the Fe I lines in LTE. Blends are treated consistently by adding the opacities of all the relevant transitions at each wavelength and spatial position, and then solving the radiative transfer equation with the total opacity. The non-LTE calculation is based on the preconditioning strategy of Rybicki and Hummer (1992) (see also Socas-Navarro and

Trujillo Bueno, 1997) assuming complete angle and frequency redistribution. This last approximation is particularly good for the Ca II infrared triplet lines, as shown by Uitenbroek (1989).

Let us consider in detail the models obtained for the points that we labeled as *A* and *B*. Figures 5 and 6 show the atmospheric stratification inside the downflows, as well as an average over the surrounding, non-downflowing area for reference. For each parameter we have chosen the smallest number of nodes that provides a reasonable fit to the observations (examples are shown in Figure 7), as determined by some trial and error and previous experience. We found that more nodes resulted in large error bars (shown in the figures at the node locations) due to uniqueness issues. We make the implicit assumption that the models are smooth enough to be properly described by the set of nodes selected.

The most striking features in the retrieved models are the strong downwards velocities found in the upper photosphere, around $\log(\tau_{500}) = -3$. The motions along the line-of-sight approach the speed of sound in point *B* and exceed it in point *A*. The other parameters show different behaviors in points *A* and *B*. In particular, the downflowing layer in point *B* is considerably hotter than the reference atmosphere. However, in point *A* the downflowing layer is cooler (although it then becomes

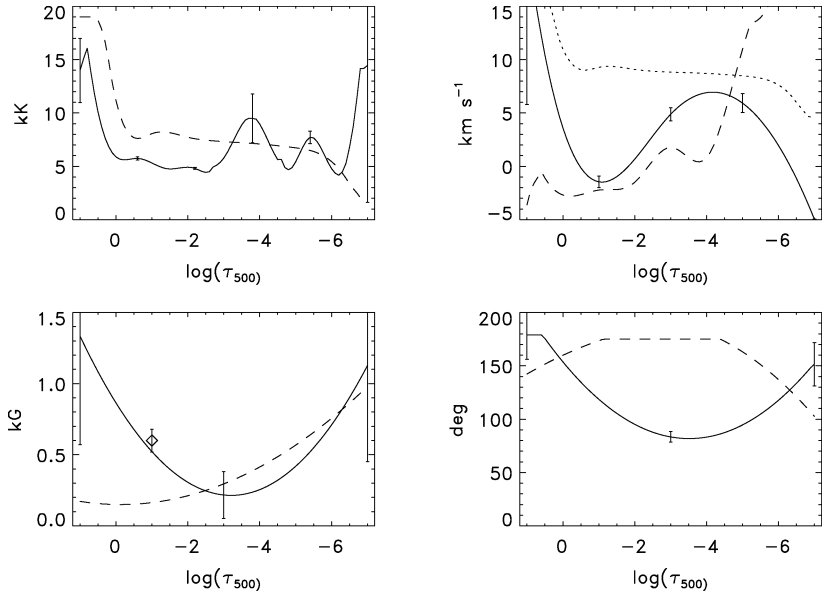

Figure 5. Average model atmosphere in the downflowing feature labeled as point *A* (*solid*) and its surroundings (*dashed*). Panels from top to bottom, left to right are temperature, line-of-sight velocity, magnetic field strength and inclination. The *dotted line* in the upper right panel represents the speed of sound in the atmosphere. The *diamond* shows the field strength retrieved from the inversion of the photospheric lines alone. *Error bars* are plotted at the *inversion nodes* (see Socas-Navarro, Trujillo Bueno, and Ruiz Cobo, 2000b, 2001 for details). The magnetic filling factor is 55%.

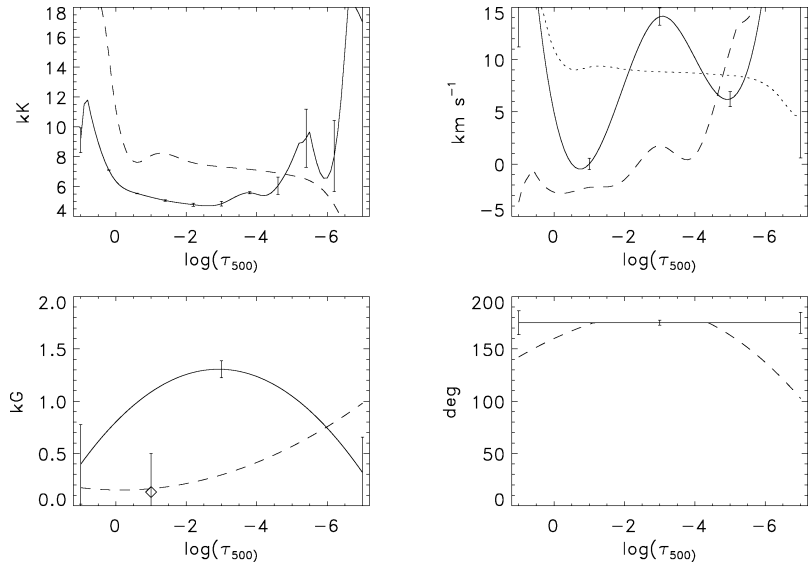

Figure 6. Average model atmosphere in the downflowing feature labeled as point *B* (*solid*) and its surroundings (*dashed*). Panels from top to bottom, left to right are temperature, line-of-sight velocity, magnetic field strength and inclination. The *dotted line* in the upper right panel represents the speed of sound in the atmosphere. The *diamond* shows the field strength retrieved from the inversion of the photospheric lines alone. The magnetic filling factor is 80%.

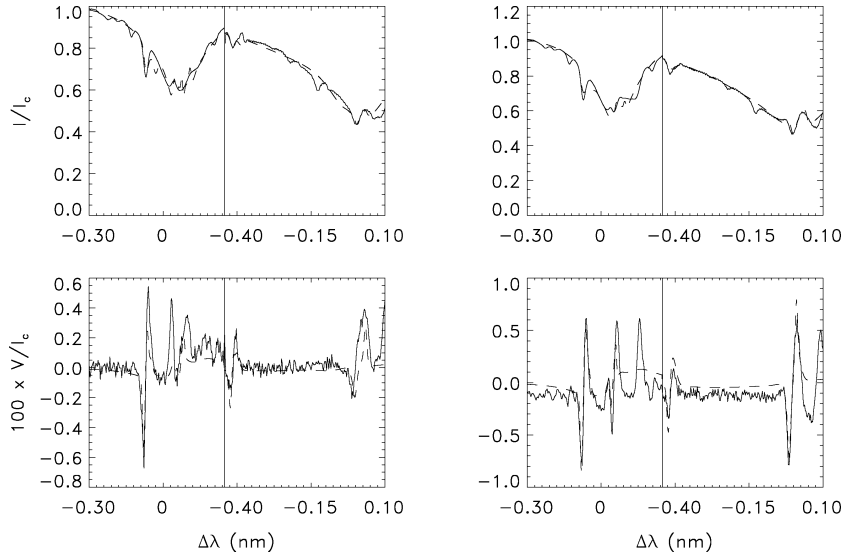

Figure 7. Fits to 849.8 and 854.2 nm (left and right side of each panel, respectively). Left and right panels represent typical profiles in the downflowing areas in the vicinity of points *A* and *B* respectively. Upper panels: Stokes *I*. *Lower panels*: Stokes *V*. In all cases the *solid* (*dashed*) line represents the observations (fits). The profiles in this figure have been averaged over a 3 × 3 pixel box to improve the signal-to-noise ratio in Stokes *V*.

hotter at higher layers). In both cases there is another hot layer at $\log(\tau_{500}) = -5$. Our findings for the two regions are consistent with the results of Georgoulis *et al.* (2002) who found EBs to be predominantly regions of downflows with no indication of upflows.

The fits provided by the inversions can be seen in Figure 7. Note that the observed chromospheric profiles exhibit a very complex structure with multiple peaks in Stokes V (the photospheric lines, on the other hand, produce rather normal profiles). Generally speaking, the inversion code yields a reasonably good fit to the overall features, but there is more structure in the observed profiles (particularly noticeable in Stokes V with multiple peaks), than in the synthetic ones. This is an indication that the actual atmospheres are even more complex than our models, probably due to the presence of unresolved atmospheric components.

The photospheric field strength shown in Figures 5 and 6 is poorly constrained because the inversion weights the Ca II lines more heavily (they span a larger wavelength range). In order to better define the photospheric field, we repeated these inversions but considering only the Fe I lines. In this case we imposed a magnetic field that is constant with height because there is not enough information in these two lines alone to retrieve more complicated variations. The field strengths obtained are overplotted as diamonds in the figures. Note that in point B the photospheric field is within the so-called *weak-field regime* (the Zeeman splitting is smaller than the Doppler width). In the absence of linear polarization it is not possible to separate the effects of field strength and filling factor, hence the larger error bar.

Thus far, we have not made a direct connection between the downflowing features analyzed here and EBs. To this end, we used the model atmospheres obtained from the inversion to synthesize the Hα profiles that these models produce. The result is plotted in Figure 8, along with a reference quiet Sun profile calculated from model C of Vernazza, Avrett, and Loeser (1981) (VAL-C). This synthetic profile has the same appearance traditionally observed in EBs. Ellerman (1917) describes the Hα spectra of those structures as having emission features (brighter than the continuum) on both sides of the line center. The red asymmetry (higher intensity peak in the red wing) shown here is not the most commonly observed in EBs (see the introduction), but this asymmetry is present quite often (40% of the cases according to Rust, 2001). It is the result of a hot downflowing component as seen in Figure 5. The resemblance of EBs (see *e.g.*, the photographic plates in Ellerman, 1917) with the profiles in Figure 8 is solid evidence that we are indeed observing the same phenomenon. Moreover, it also provides strong support for the reliability of the inversions.

When compared to previous published Hα line profiles of EBs (Bruzek, 1972; Kitai, 1983), our profiles have somewhat narrower emission peaks. This difference might arise from complexities of the hydrogen line formation not included in our Hα synthesis (*e.g.*, partial redistribution effects), or it could simply mean that we are observing a slightly different process.

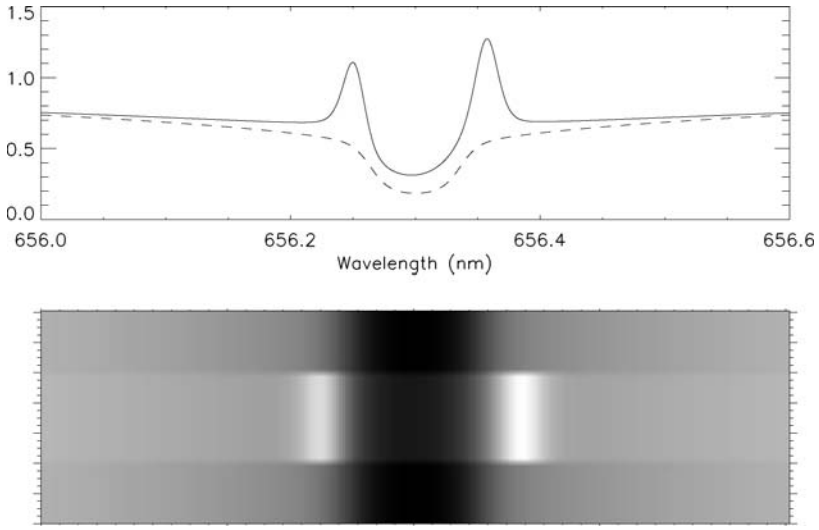

Figure 8. Upper panel: Synthetic Hα profiles obtained with the model atmosphere from the inversion of point *A* (*solid*) and the VAL-C model (*dashed*). Point *B* produced a qualitatively similar profile. *Lower panel*: Simulation of the appearance of slit spectra using the profiles in the *upper panel* to allow for easy comparison with the photographic plates published by Ellerman (1917).

4. Conclusions

The energetic phenomenon generally referred to as an EB has remained very poorly understood to solar physicists for almost a century. This is probably due in no small measure to the fact that it has only been observed in Hα thus far, which is a very difficult line to interpret. In this paper we present the first observations of EBs in other lines, namely the Ca II infrared triplet. These lines are much easier to model and have been successfully inverted in the past few years (*e.g.*, Socas-Navarro, Trujillo Bueno, and Cobo, 2000a, 2001; Socas-Navarro, 2005b) and thus our results open a new window to the observational study of EBs.

We find that the EBs analyzed in this work are associated with supersonic (or nearly so) downflows in the upper photosphere. No upflows are observed in our data. Socas-Navarro (2005a) determined the vector current densities in the large sunspot of Figure 1 and found that the western penumbra is permeated by strong currents in the upper photosphere, with a magnitude of $\sim 3 \times 10^5$ A km^{-2}. The fact that these EBs occur in a region with strong currents suggests that EBs may be associated with magnetic reconnection.

The relatively strong chromospheric fields are not too surprising since the points analyzed are immediately adjacent to a sunpot. In any case, a hard lower limit to the magnetic field may be obtained from the total flux (which is determined more or less straightforwardly by the Stokes V amplitudes of the Ca II lines), resulting in $\sim$400 G for point *A* and $\sim$300 G for point *B*.

In order to understand the nature of EBs and the physical processes that produce them, it would be extremely valuable to have time-series observations of photospheric and chromospheric lines, ideally with full Stokes polarimetry.

Acknowledgments

The authors wish to acknowledge the enthusiastic support from the NSO staff at Sacramento Peak, especially D. Gilliam, M. Bradford, and J. Elrod. Thanks are also due to S. Hegwer, S. Gregory, R. Dunbar, T. Spence, S. Fletcher, C. Berst, and W. Jones.

References

Bruzek, A.: 1972, *Solar Phys.* **26**, 94.
Dara, H.C., Alissandrakis, C.E., Zachariadis, T.G., and Georgakilas, A.A.: 1997, *Astron. Astrophys.* **322**, 653.
Ellerman, F.: 1917, *Astrophys. J.* **46**, 298.
Georgoulis, M.K., Rust, D.M., Bernasconi, P., and Schmieder, B.: 2002, *Astrophys. J.* **575**, 506.
Harvey, J. and Harvey, K.: 1973, *Solar Phys.* **28**, 61.
Kitai, R.: 1983, *Solar Phys.* **87**, 135.
Koval, A.N. and Severny, A.B.: 1970, *Solar Phys.* **11**, 276.
Litvinenko, A.: 1999, *Astrophys. J.* **515**, 435.
Nindos, A. and Zirin, H.: 1998 *Solar Phys.* **182**, 381.
Pariat, E., Aulanier, G., Schmieder, B., Georgoulis, M. K., Rust, D.M., and Bernasconi, P.: 2004 *Astrophys. J.* **614**, 1099.
Qiu, J., Ming, D.D., Wang, H., Denker, C., and Goode, P.R.: 2000 *Astrophys. J.* **544**, L157.
Ren, D., Hegwer, S.L., Rimmele, T., Didkovsky, L.V., and Goode, P.R.: 2003, in S.L. Keil and S.V. Avakyan (eds.), *Innovative Telescopes and Instrumentation for Solar Astrophysics*. Proceedings of the SPIE, **4853**, 593.
Rust, D.M. and Keil, S.L.: 1992, *Solar Phys.* **140**, 55.
Rust, D.: 2001, *Encycl. Astron. Astrophys.*, E2263R.
Rybicki, G.B. and Hummer, D.G.: 1992, *Astron. Astrophys.* **262**, 209.
Shimizu, T., Shine, R.A., Title, A., Tarbell, T., and Frank, Z.: 2002, *Astrophys. J.* **574**, 1074.
Socas-Navarro, H.: 2005a, *Astrophys. J.* **633**, L57.
Socas-Navarro, H.: 2005b, *Astrophys. J.* **631**, L167.
Socas-Navarro, H., Elmore, D., Pietarila, A., Darnell, A., Lites B.W., and Tomczyk, S.: 2006, *Solar Phys.* **235**, 55.
Socas-Navarro, H., Ruiz Cobo, B., and Trujillo Bueno, J.: 1998, *Astrophys. J.* **507**, 470.
Socas-Navarro, H. and Trujillo Bueno, J.: 1997, *Astrophys. J.* **490**, 383.
Socas-Navarro, H., Trujillo Bueno, J., and Ruiz Cobo, B.: 2000a, *Science* **288**, 1396.
Socas-Navarro, H., Trujillo Bueno, J., and Ruiz Cobo, B.: 2000b, *Astrophys. J.* **530**, 977.
Socas-Navarro, H., Trujillo Bueno, J., and Ruiz Cobo, B.: 2001, *Astrophys. J.* **550**, 1102.
Uitenbroek, H.: 1989, *Astron. Astrophys.* **213**, 360.
Vernazza, J.E., Avrett, E.H., and Loeser, R.: 1981, *Astrophys. J. Suppl.* **45**, 635.